

High resolution wind-tunnel investigation about the effect of street trees on pollutant concentration and street canyon ventilation

*Original*

High resolution wind-tunnel investigation about the effect of street trees on pollutant concentration and street canyon ventilation / Fellini, Sofia; Marro, Massimo; DEL PONTE, ANNIKA VITTORIA; Barulli, Marilina; Soulhac, Lionel; Ridolfi, Luca; Salizzoni, PIETRO STEFANO. - In: BUILDING AND ENVIRONMENT. - ISSN 0360-1323. - 226:(2022), p. 109763. [10.1016/j.buildenv.2022.109763]

*Availability:*

This version is available at: 11583/2974160 since: 2022-12-24T12:15:23Z

*Publisher:*

Elsevier

*Published*

DOI:10.1016/j.buildenv.2022.109763

*Terms of use:*

This article is made available under terms and conditions as specified in the corresponding bibliographic description in the repository

*Publisher copyright*

(Article begins on next page)

1 Wind-tunnel investigation about the effect of street  
2 trees on canyon ventilation

3 Sofia Fellini<sup>a,\*</sup>, Massimo Marro<sup>a</sup>, Annika Vittoria Del Ponte<sup>b</sup>, Marilina  
4 Barulli<sup>b</sup>, Lionel Soulhac<sup>a</sup>, Luca Ridolfi<sup>b</sup>, Pietro Salizzoni<sup>a</sup>

5 <sup>a</sup>*Univ Lyon, INSA Lyon, CNRS, Ecole Centrale de Lyon, Univ Claude Bernard Lyon 1,*  
6 *LMFA, UMR5509, 69621, Villeurbanne France*

7 <sup>b</sup>*Department of Environmental, Land, and Infrastructure Engineering, Politecnico di*  
8 *Torino, Corso Duca degli Abruzzi 24, 10129 Turin, Italy*

---

9 **Abstract**

10 Greening cities is a key solution to improve the urban microclimate and mit-  
11 igate the impact of climate change. However, the effect of tree planting on  
12 pollutant dispersion in streets is still a debated topic. To shed light on this  
13 issue, we present a wind-tunnel experiment aimed at investigating the effect of  
14 trees on street canyon ventilation. An idealized urban district was simulated  
15 by an array of blocks, and two rows of model trees were arranged at the sides  
16 of a street canyon oriented perpendicularly with respect to the wind direction.  
17 Reduced scale trees were chosen to mimic a realistic shape and aerodynamic be-  
18 haviour. Three different spacings between the trees were considered. A passive  
19 scalar was injected from a line source placed at ground level and concentration  
20 measurements were performed in the whole canyon. Results show that the pres-  
21 ence of trees alters the concentration field in the street with a progressive shift  
22 from a nearly two-dimensional to a three-dimensional field depending on tree  
23 density. The main finding is that, despite the significant spatial variability of  
24 the mean concentration induced by the trees, their presence does not affect the  
25 overall ventilation efficiency as the bulk exchange velocity between the street  
26 canyon and the overlying atmosphere remains almost constant in the different  
27 configurations.

---

\*Corresponding author

Email address: sofia.fellini@ec-lyon.fr (Sofia Fellini)

## 28 **Introduction**

29 Urban vegetation plays a key role for the livability of cities (Bozovic et al.,  
30 2017). Beyond its aesthetic role, the presence of vegetation brings numerous  
31 environmental benefits in urban areas. Evapotranspiration and shading have  
32 cooling effects that mitigate the urban heat island (Oliveira et al., 2011; Geor-  
33 gakis and Santamouris, 2017). The large surface area per unit volume of vege-  
34 tative structures facilitates particle deposition which acts as a sink for pollutant  
35 particles (Litschke and Kuttler, 2008). Moreover, vegetation has a fundamen-  
36 tal role in the hydrological cycle: water infiltration in vegetated soils retains  
37 stormwater from entering the drainage system, thus reducing the risk of flash  
38 floods (Livesley et al., 2016; Busca and Revelli, 2022).

39 While the social and environmental benefits of vegetation in cities are well  
40 recognized, the role of vegetation on pollutant dispersion is still controversial  
41 (Janhäll, 2015) and depends on the non-trivial interaction between the flow  
42 field, the vegetative elements, and the surrounding built environment (Abhijith  
43 et al., 2017). This is particularly true in street canyons, where the turbulent  
44 flow field is strongly influenced by the geometry of the canyon, its orientation  
45 with respect to the external wind (Soulhac et al., 2008), the presence of ob-  
46 stacles (Buccolieri et al., 2022), and the properties of the building walls, e.g.,  
47 wall roughness and temperature (Allegrini et al., 2013; Murena and Mele, 2016;  
48 Marucci and Carpentieri, 2019; Fellini et al., 2020). The presence of vegetated  
49 façades on the building walls, for example, alters the near-wall velocity and may  
50 result in a reduction of the turbulent air exchange (Li et al., 2022). Low-level  
51 hedges, instead, generally improve the air quality at street level and thus help  
52 reducing the dose of pollutants inhaled by pedestrians (Gromke et al., 2016).

53 The interaction between turbulent flow and vegetation is even more complex  
54 in tree-lined avenues, where trees occupy a significant volume of the canyon and  
55 their effect on pollutant dispersion depends on the properties and shape of the  
56 crowns, the height of the trunks, and the planting pattern (Vos et al., 2013;  
57 Huang et al., 2019). A pioneering series of wind-tunnel experiments was per-

58 formed by Gromke and Ruck (2007, 2009, 2012) to investigate this scenario. In  
 59 their first studies, trees were modelled as a row of small-scale trees with spher-  
 60 ical, permeable crowns on thin stems, placed in the middle of a street canyon  
 61 of unit height to width ratio  $H/W$  (Gromke and Ruck, 2007). The wind was  
 62 perpendicular to the canyon axis. The flow field within the canyon and the  
 63 concentration at the canyon walls were explored by varying different properties  
 64 of the trees (crown diameter, tree height, tree spacing). A relevant increase of  
 65 concentration at the upwind wall and a slight decrease of concentration at the  
 66 downwind wall were observed. These variations were more marked when the  
 67 canyon was occupied by the greatest volume of vegetation (large diameter of  
 68 crowns and small distance between the trees). To better investigate the effect  
 69 of tree crown porosity, in a later study, trees were replaced with a metallic cage  
 70 filled with different amounts of synthetic wadding material (Gromke and Ruck,  
 71 2009). They found that concentrations are sensitive to crown porosity only for  
 72 high porosity values ( $> 97\%$ ). Adopting the same experimental conditions, Buc-  
 73 colieri et al. (2009, 2011) simulated a large street canyon ( $H/W = 0.5$ ) with two  
 74 rows of trees. They also analysed the case of an approaching wind inclined by  
 75  $45^\circ$  with respect to the street axis. The aspect ratio of the canyon and the wind  
 76 direction turned out to be more influential with respect to vegetation density  
 77 and crown porosity. However, they evidenced that neglecting the presence of  
 78 vegetation in the streets would lead to significant errors in the predictions of  
 79 concentration levels.

80 The modification of the airflow and concentration field within streets due to  
 81 tree planting has been widely studied also by means of numerical simulations.  
 82 Reynolds-averaged Navier-Stokes (RANS) models proved to be able to qualita-  
 83 tively reproduce the experimental results (e.g. Gromke et al., 2008; Buccolieri  
 84 et al., 2009, 2011; Gromke and Blocken, 2015; Vranckx et al., 2015) but Large  
 85 Eddy Simulations provide a better agreement as they solve the intermittent and  
 86 unsteady fluctuations of the turbulent flow which plays a major role in venti-  
 87 lation dynamics (e.g., Salim et al., 2011; Moonen et al., 2013). However, the  
 88 advantages of LES involve higher computational costs that can increase by an

89 order of magnitude compared to RANS (Salim et al., 2011). Merlier et al. (2018)  
90 showed that, thanks to its computational efficiency, LES with the lattice Boltz-  
91 mann method (LBM) is a promising technique to predict dispersion in street  
92 canyons with tree plantings.

93 Despite remarkable advances in numerical models, simulating complex and  
94 porous geometries such as trees and their effect on pollutant dispersion still rep-  
95 resents a challenge. Wind-tunnel experiments are thus highly recommended to  
96 improve and validate existing models. To our knowledge, there is currently no  
97 experimental dataset that provides a complete characterization of the concen-  
98 tration field in a three-dimensional street canyon with different configurations of  
99 tree planting. For these reasons, we present in this work the results from a wind-  
100 tunnel experiment aimed at evaluating how tree planting influences the concen-  
101 tration field within a street canyon. To this aim, we reproduce a street canyon  
102 oriented perpendicular with respect to the wind direction, with two lateral rows  
103 of trees and a linear source of gas to mimic vehicular emissions. To provide  
104 a detailed description of the phenomenon, the concentration field is measured  
105 on a high-refined measurement grid with around 1000 sampling points for each  
106 configuration of tree density. The reference configuration is that of a canyon  
107 closed laterally, i.e. it does not communicate with side streets. Although this  
108 is an uncommon configuration, it allows us to accurately estimate the exchange  
109 of pollutants between the canyon and the atmosphere above. Experiments have  
110 however also been performed in a laterally open canyon, showing that the spatial  
111 pattern of concentration is not significantly affected by the presence of lateral  
112 openings.

113 In Section 1, the experimental setup and the adopted measurement tech-  
114 niques are presented. In Section 2, we discuss the similarity criteria for the  
115 aerodynamic modelling of trees and for the boundary layer in the wind tunnel.  
116 The characterization of the concentration field in the street canyon is reported  
117 in Section 3, together with the estimate of the ventilation efficiency. Moreover,  
118 the effect of lateral conditions due to different extremities (street intersections,  
119 open or closed canyon) is discussed in Section 4. Finally, the conclusions and

perspectives of the work are presented in Section 5.

## 1. Experimental setup and measurement techniques

### 1.1. Wind-tunnel setup

The experiments were performed in the atmospheric wind tunnel at the laboratory Laboratoire de Mécanique des Fluides et d’Acoustique (LMFA) at the École Centrale de Lyon. The aerodynamic circuit is composed by an axial fan which induces wind velocities between 0.5 and 6 m/s, flow diverging and converging systems, and an upwind grid for the generation of homogeneous turbulence. A heat exchanger system regulates the air temperature with a precision of 0.5 K. The test section of the wind tunnel is 12 m long, 3.5 m wide, and 2 m high.

To simulate an idealized urban district (Fig. 1), the floor of the entire test section was overlaid with an array of square blocks (panel a in Fig. 2). The blocks were 50 cm wide and 10 cm high and made of wood and polystyrene. The spacing between the obstacles was 10 cm in the spanwise direction and 20 cm in the lengthwise direction. In this way, we obtained a street network composed of square canyons (height to width ratio  $H/W = 1$ ) aligned with the wind direction intersecting larger perpendicular streets ( $H/W = 0.5$ ). The two different proportions were selected to avoid channeling effects along the wind direction and to recreate tree-lined boulevards in the direction perpendicular to the wind. The blockage ratio of the model to the cross-section of the wind tunnel was 5%.

A neutrally stratified boundary layer approximately 1.1 m depth was generated by combining the effect of a row of 0.95 m high Irwin spires (Irwin, 1981), placed at the beginning of the test section, and the building-like obstacles on the floor. Moreover, the obstacles were covered by 5 mm high bolts to generate further roughness and accelerate the full development of the boundary layer. The free stream velocity at the top of the boundary layer ( $U_\infty$ ) was kept constant around 5 m/s. More details about the boundary layer above the obstacles

149 is given in Section 2.2.

150 The reference street canyon (see photo reported in Fig. 2.c) was placed  
151 perpendicular to the wind direction, at a distance of approximately 9 meters  
152 from the beginning of the test section. Its length (L), width (W), and height  
153 (H) measured 1.0 m, 0.2 m, and 0.1 m, respectively (Fig. 2.b and d). In a 1:200  
154 scale, the street canyon matches fairly well a typical tree-lined boulevard, 40 m  
155 wide and flanked by 20 m high buildings, as in typical European city centres  
156 (e.g., Barcelona, Turin, Lyon). Note that, in the experiment, the length of the  
157 canyon does not cover the whole width of the test section. This choice is made  
158 in order to define a control volume in which to apply the mass balance for an  
159 accurate estimate of the ventilation efficiency (see Section 3.2). We are aware  
160 that other boundary conditions are possible, for instance street intersections or  
161 an indefinitely long canyon. The effects of different lateral extremities will be  
162 discussed in Section 4.

163 To simulate urban vegetation in the street canyon, model trees were aligned  
164 along two lateral rows 14 cm apart. Three different configurations for the tree  
165 density were analysed: in configuration *Zero* (panel d), the street canyon was  
166 empty. In configuration *Half* (panel e), seven equally spaced trees were arranged  
167 along each lateral row. In configuration *Full* (panel f), the lateral rows were  
168 composed of fourteen trees with no space between them. The aerodynamic  
169 characterization of model trees is reported in Section 2.1.

170 To simulate vehicular emissions, a tracer was emitted by a linear source at the  
171 centre of the reference street canyon. The source consisted of a stainless steel  
172 tube pierced with needles emitting ethane in a gas homogenization chamber,  
173 located in a slot cut in the tunnel floor. From this chamber the gas was released  
174 homogeneously at street level from a 65 cm long and 1 cm wide metallic grid.  
175 This design aims at minimizing the vertical momentum and maximize the lateral  
176 homogeneity of the emission (Meroney et al., 1996; Marro et al., 2020). Ethane  
177 was chosen as a tracer, since it has approximately the same density of air (the  
178 density ratio between ethane and air being about 1.03). The source released a  
179 mixture of air and ethane with a total flow rate of 4 l/min and thus a negligible



Figure 1: (a) Aerial view of the city of Barcelona (Spain). Source: *Barcelona From Above* by Ian Harper. (b) The modelled urban canopy in the wind tunnel.

180 injection velocity at street level of approximately 0.01 m/s. The percentage of  
 181 ethane was around 5% in volume, corresponding to a flow rate of around 0.2  
 182 l/min. The supply of the two gases was monitored by two digital mass-flow  
 183 controllers (Alicat Scientific MC-Series) working in a range between 0.5 and 20  
 184 Nl/min.

### 185 1.2. Measurement techniques

186 The concentration field within the reference street canyon was measured  
 187 using a Flame Ionisation Detector (FID) system (Fackrell, 1980), which is com-  
 188 monly used for measurements in urban-like geometries (Pavageau and Schatz-  
 189 mann, 1999; Carpentieri et al., 2012; Fellini et al., 2020). To avoid the disruption  
 190 of the local flow, a straight 30 cm long sampling capillary tube was mounted on  
 191 the FID head, which was positioned above the test section so as not to affect  
 192 the flow field. The sampling frequency of the FID signal was fixed at 1000 Hz  
 193 (Nironi et al., 2015). The instrument works in the range 0-10 Volt and it can  
 194 detect concentration values between 0 and 5000 ppm with an accuracy of about  
 195 1-2 ppm.

196 The measurements were performed in statistically steady conditions: a con-  
 197 stant flow rate of ethane was injected from the ground level source and the  
 198 concentration within the cavity was measured at around 1000 sampling points



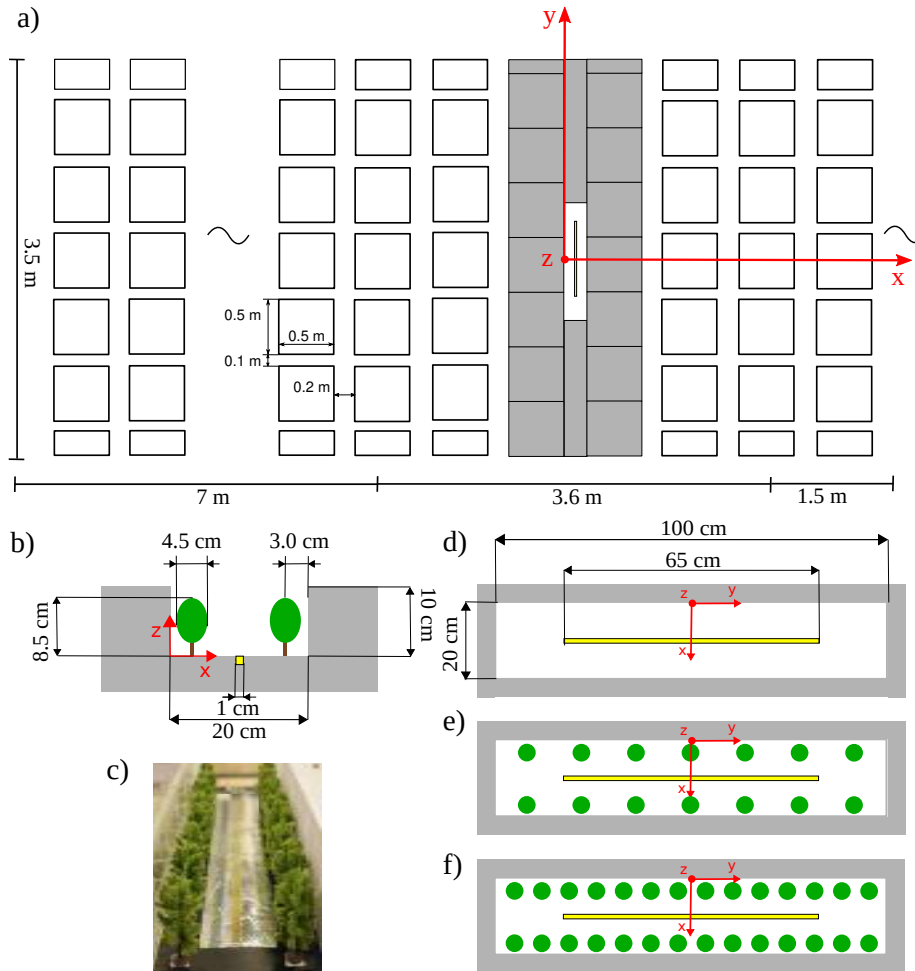


Figure 2: (a) Sketch of the urban canopy in the test section of the tunnel. The blocks delimiting the reference street canyon are coloured grey. Sketch (b) and photo (c) of the front view of the street. Top view of the street canyon model for the different configurations of tree density: (d) *Zero*, (e) *Half*, (f) *Full*. The yellow line represents the pollutant source

199 for each configuration of tree density. The measurement grid was defined to  
200 characterize the entire three-dimensional volume in detail (see Fig. 1 in the  
201 Supplementary Material). For each point, we fixed a sampling time of 2 min-  
202 utes which provides a reliable estimate of the mean concentration. Moreover,  
203 before and after each acquisition, the background concentration was recorded  
204 by stopping the emission for 15 seconds (and leaving time for the transients to  
205 settle). The background concentration, which was assumed to evolve linearly  
206 with time from its initial to its final value, was then subtracted from the signals  
207 (Marro et al., 2020; Vidali et al., 2022).

208 The velocity field above the obstacles was characterized (Section 2.2) by  
209 means of a Hot-Wire Anemometer (HWA) at constant temperature, using an  
210 X-wire probe with acceptance angle of  $45^\circ$ . In this way, two velocity components  
211 of the velocity field were measured simultaneously. The platinum probe wire was  
212 1 mm long and with a diameter of  $5\text{ }\mu\text{m}$ . The small size of the hot-wire element  
213 enables good spatial resolution of the velocity field while the low thermal inertia  
214 of the material ensures fast response, allowing the detection of high-frequency  
215 fluctuations of the turbulent flow (Comte-Bellot, 1976). An acquisition time of  
216 1 minute at a frequency of 4000 Hz was adopted for each sampling point.

217  
218 For the aerodynamic characterization of the model trees (presented in Sec-  
219 tion 2.1), their drag coefficient was measured in a small closed-circuit wind  
220 tunnel with a 30 cm x 30 cm test section and able to generate velocities up to  
221 25 m/s. The tunnel was equipped with an external load cell with a precision of  
222 0.01 N. Different layouts of trees were attached to a removable plate connected  
223 with the load cell. The drag coefficient was estimated for a varying wind velocity  
224 inside the tunnel. Moreover, the aerodynamic porosity of the model trees was  
225 evaluated by performing velocity measurements upwind and downwind a single  
226 tree on a regular grid by means of a Pitot tube.

## 227 2. Similarity criteria

### 228 2.1. Aerodynamic characterization of model trees

229 To investigate the effect of trees in urban areas by means of wind-tunnel  
230 experiments, buildings and vegetative structures need to be modelled in small  
231 scale. Similarity criteria are then necessary to transfer small-scale findings in  
232 the wind tunnel to full-scale applications. For impermeable and rigid structures,  
233 like buildings, dynamical similarity between the experiment and the real appli-  
234 cation exists if the model and the full-scale object are geometrically similar and  
235 the value of the Reynolds number is the same (Tritton, 2012). In case of fully  
236 turbulent flows around bluff bodies and/or with complex geometries, this con-  
237 dition is weakened and flow similarity is assumed as far as the Reynolds number  
238 is sufficiently large. On the other hand, less knowledge is available about the  
239 appropriate similarity criteria for vegetative structures. From a fluid dynamical  
240 point of view, vegetation is a complex porous medium made of branches and  
241 leaves giving rise to the development of boundary layers, wakes, and recircula-  
242 tion zones (Gromke and Ruck, 2008). Moreover, due to their flexibility, trees  
243 can sway with the wind and induce fluid-structure interactions.

244 In previous wind-tunnel experiments, trees, windbreaks, and canopies have  
245 been modelled by using different materials, e.g., brushes, cotton balls, metal  
246 screens, and plastic stripes. Aerodynamic validation of the adopted structures  
247 was done by analysing different fundamental features of the interaction between  
248 the trees and the flow field, as the drag coefficient, the characteristics of the  
249 wakes behind the trees (Meroney, 1968), the ratio between tree height and  
250 roughness length (Meroney, 1980), the leaf area density (Chen et al., 1995), or  
251 the sway frequency (Stacey et al., 1994). More systematically, Gromke and Ruck  
252 (2008) analysed the aerodynamic characteristics of 12 small-scale modelled trees  
253 made of different materials and porosity. Measurements of the drag coefficient  
254 and of the flow field around the crowns evidenced the drag coefficient as a key  
255 scale parameter for the modelling of trees. Manickathan et al. (2018) compared  
256 the aerodynamic behaviour of model and natural trees in a wind tunnel. They

found that, together with the drag coefficient, the aerodynamic porosity of the tree crown is another key parameter to compare natural and model trees.

In accordance with these studies, we mimicked natural trees with plastic trees for railway modelling and we characterized their aerodynamic behaviour by estimating their aerodynamic porosity and their drag coefficient. We also investigated their optical porosity. The trees were 8.5 cm high ( $h_T$ ) and 4.5 cm wide ( $w_T$ ), with crowns in plastic porous material on plastic trunks. Under the conditions of the experiment, tree models behaved like rigid bodies and thus deformations and fluid-structure interactions could be neglected.

Aerodynamic porosity ( $\alpha_p$ ) is defined (Guan et al., 2003) as the ratio of the time average wind speed behind the obstacle ( $U_b$ ) and the average speed of the approaching wind ( $U_{ref}$ ):

$$\alpha_p = \frac{\int_{A_c} U_b(x, y) dA_c}{\int_{A_c} U_{ref}(x, y) dA_c}, \quad (1)$$

where  $A_c$  is the projected frontal area of the obstacle. In other words, aerodynamic porosity determines the portion of the flow that passes through the porous material with respect to the flow that diverges from the obstacle. To estimate  $\alpha_p$ , we performed velocity measurements upstream and downstream a single tree that was placed on a raised block in the wind tunnel so that the incident flow was not affected by the boundary layer and the integral at the denominator in Eq. 1 could be replaced by the simple product  $U_{ref} \cdot A_c$ . Behind the tree (in the first plane not occupied by the tree branches) point velocities were measured on a regular and dense grid and a two-dimensional velocity field was obtained through spatial interpolation. The average velocity was then estimated by integrating the velocity field over the tree silhouette (Fig. 3.b). The mean speed upstream ( $U_{ref}$ ) and downstream ( $U_b$ ) the tree were 4.95 m/s and 1.48 m/s, respectively. By means of Eq. 1, we obtained  $\alpha_p = 0.3$ , a value in line with that of common natural trees, as hollies and cypresses (see square markers in Fig. 3.d from the study of Manickathan et al. (2018)).

The optical porosity  $\beta_p$  is another commonly used parameter to characterize the vegetation and it can be easily estimated by elaborating digital photos (Velarde et al., 2018). It is defined as the ratio between the open surface of a porous material and its total surface. Through a digital elaboration of the photo capturing the frontal view of the model tree (Fig. 3.a), we delimited the silhouette of the tree and obtained its cross-section,  $A_c \approx 3.5 \times 10^{-3} \text{ m}^2$ . Then, we estimated the optical porosity,  $\beta_p \approx 0.05$ , as the ratio of the number of white pixels to the total number of pixels within the silhouette of the tree. According to the empirical relationship found experimentally by Guan et al. (2003), the optical porosity ( $\beta_p$ ) is related to the aerodynamic porosity as:

$$\alpha_p \simeq \beta_p^n, \quad (2)$$

where the exponent  $n$  was estimated by Guan et al. (2003) equal to 0.4 for realistic windbreak. Introducing our estimated values for  $\alpha_p$  and  $\beta_p$  in Eq. 2, we find  $n \approx 0.402$  that is consistent with the cited study. The relation in Eq. 2 can then be conveniently used for deriving the aerodynamic porosity when velocity measurements cannot be directly performed.

The drag coefficient is defined as:

$$c_d = \frac{2F}{\rho_a U_{ref}^2 A_c}, \quad (3)$$

where  $F$  is the drag force [N],  $\rho_a$  is air density [ $\text{kg}/\text{m}^3$ ],  $U_{ref}$  is the reference velocity [m/s] for the approaching wind, and  $A_c$  is the projected frontal area of the tree [ $\text{m}^2$ ]. The drag force  $F$  was measured by means of a load cell, while the velocity  $U_{ref}$  was measured with a Pitot tube, as explained in Section 1.2.

In Fig. 3.b, we report the drag coefficient as a function of the wind velocity  $U_{ref}$  and Reynolds number  $Re$  for four different faces of a single model tree, obtained by rotating the vertical axis of the tree at intervals of  $90^\circ$ . The Reynolds number was calculated as  $Re = U_{ref} H_T / \nu$ , where  $H_T$  is the tree height and  $\nu$  is the air kinematic viscosity ( $\nu \approx 1.55 \times 10^{-5} \text{ m}^2/\text{s}$  at a temperature of  $25^\circ\text{C}$ ). Except for the values at low speed (where the experimental uncertainty of the

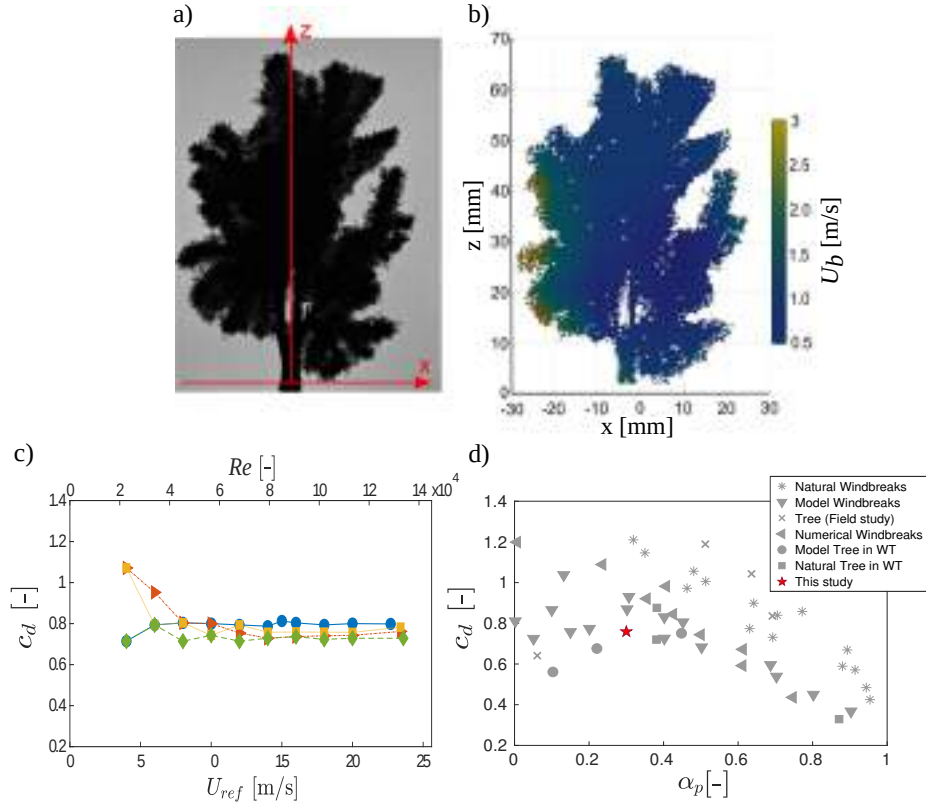


Figure 3: a) Front photo of the model tree. b) 2D velocity field downstream the tree obtained by spatial interpolation of point velocity measurements for the estimation of  $\alpha_p$ . c) Drag coefficient as a function of Reynolds number and wind velocity for four different positions (reported by different colours) of a single model tree, obtained by rotating the vertical axis of the tree at  $90^\circ$  intervals. b) Drag coefficient and aerodynamic porosity for various model trees and natural trees. From the study of Manickathan et al. (2018).

measurement is large), the drag coefficient rapidly converges to a constant value around 0.75. As shown in Fig. 3.d, this value is in line with the drag coefficient of natural trees and confirms that the model trees adopted in this study present realistic aerodynamic properties.

We note that natural trees undergo foliage reconfiguration and their drag coefficient decays with increasing wind speed (Manickathan et al., 2018). This is not found in our model trees that do not deform. However, since in this study we focus on moderate velocities in a street canyon, we are not interested in reproducing the flexibility of natural trees.

## 2.2. Characterization of the boundary layer

To characterize the wind flow over the obstacles, we measured vertical velocity profiles in different positions of the wind tunnel.

The evolution of the boundary layer along the central axis of the wind tunnel (from  $x = -1.27$  m to  $x = 1.27$  m) is shown in the right part of Fig. 4.a (blue top  $x$ -axis). The good overlapping between the curves reveals that the flow is fully developed when it approaches the reference canyon ( $x = 0$ ), i.e. its development in the stream-wise direction is so slow that changes over the fetch can be neglected. As already introduced in Section 1.1, the height of the boundary layer ( $\delta$ ) is around 1.1 m, while the free-stream velocity ( $U_\infty$ ) is around 5 m/s. The characteristic Reynolds numbers based on the obstacle height are  $Re_\infty = U_\infty H / \nu \approx 3.3 \times 10^4$  and  $Re_H = U_H H / \nu \approx 1.25 \times 10^4$ , where  $U_H$  is the mean horizontal velocity at  $z = H$ . These values are sufficiently high to ensure fully-developed turbulent flow. For a square cavity, Allegrini et al. (2013) obtained a Reynolds independent flow for  $Re_\infty$  above  $1.3 \times 10^4$ , while Castro and Robins (1977) and Marucci and Carpentieri (2019) showed that the condition was met for  $Re_H$  larger than 4000.

Four velocity vertical profiles were measured at different positions within a periodic unit of the urban canopy (see the inset and the velocity profiles on the left side of Fig. 4.a, red bottom  $x$ -axis). The influence of the single obstacles is evident in the lower part of the velocity profiles (i.e. the roughness sublayer)

where a high scatter can be observed up to  $z = 0.15\delta$ . Above this height, the inertial sublayer develops and the flow variables depend on the vertical coordinate only. In this zone, the mean velocity profile is usually modelled by the logarithmic law:

$$\frac{U}{u_*} = \frac{1}{\kappa} \ln \frac{z-d}{z_0}, \quad (4)$$

where  $z_0$  is the aerodynamic roughness,  $d$  is the zero-plane displacement, and  $u_*$  is the friction velocity. In the literature, several techniques have been developed to determine the values of these parameters (Raupach et al., 2006). Here, we compare the results from two different methods.

In the first method (Salizzoni et al., 2008), the values of the three parameters were selected so as to minimize the sum of the square difference between the logarithmic velocity profile and the measurements (Fig. 4.b). The logarithmic profile only applies to a fraction of the full velocity profile. Moreover, in urban boundary layers, the inertial sublayer is squeezed by the roughness sublayer that, as seen above, extends beyond the height of the obstacles. This fact makes the delimitation of the inertial zone even more complex than in boundary layers developing over smooth or slightly rough walls. For these reasons, we explored different extensions of the fitted region in the range  $0.15 < z/\delta < 0.4$ . The resulting parameters were estimated equal to  $u_*/U_\infty = 0.051$ ,  $z_0/\delta = 9 \times 10^{-4}$ , and  $d/\delta = 0.085$ .

In the second method, the friction velocity  $u_*$  was inferred from the vertical profile of the Reynolds shear stress  $-\overline{u'w'}$ , where  $u'$  and  $w'$  are the turbulent fluctuations of the horizontal and vertical velocity, respectively. Except for a thin layer close to the wall, where viscous effects are dominant, the total stress ( $\tau = \rho_a u_*^2$ ) in the surface layer almost matches with the Reynolds stress, which is observed to be almost constant in this layer. Thus, we can write:  $\tau = \rho_a u_*^2 = -\rho_a \overline{u'w'}$ . Following this method, we have analysed the vertical profile of the Reynolds stresses (Fig. 4.c) which was obtained as a spatial average over the four horizontal positions reported in the inset of Fig. 4.a. A constant-stress region (red filled markers) was detected for  $0.14 < z/\delta < 0.36$  and the



350 corresponding  $u_*/U_\infty$  was evaluated equal to 0.046. We note that varying the  
 351 extension of the considered constant-stress region in the range  $H/\delta < z/\delta < 0.4$ ,  
 352 slight changes (of the order of 4 %) in the estimated value of  $u_*/U_\infty$  are found.  
 353 The aerodynamic roughness ( $z_0/\delta = 5 \times 10^{-4}$ ) and the zero-plane displacement  
 354 ( $d/\delta = 0.1$ ) were then estimated through a linear regression of the logarithmic  
 355 law in the semi-log domain.

356 The results from the two methods are slightly different but in line with  
 357 previous experimental studies (Rafailidis, 1997; Salizzoni et al., 2008; Garbero  
 358 et al., 2010). However, since the Reynolds stresses measured by a  $45^\circ$  X-probe  
 359 HWA are usually underestimated by about 10%-20% (Tutu and Chevray, 1975;  
 360 Cheng et al., 2007; Marro et al., 2020), we adopt the parameters estimated by  
 361 minimum mean square error, namely (in non-normalized values)  $u^* = 0.29$  m/s,  
 362  $d = 0.09$  m,  $z_0 = 1 \times 10^{-3}$  m.

363

The vertical profiles of the standard deviation of the velocity components  
 ( $\sigma_u$ ,  $\sigma_v$ , and  $\sigma_w$ ) and of the turbulent kinetic energy ( $k$ ) are reported in Figs. 4.d  
 and e. The profiles are representative of a well developed urban boundary layer  
 (Garbero et al., 2010) and can be useful for the implementation and validation  
 of CFD simulations. To this aim, we also provide in Fig. 4.f the vertical profile  
 of the turbulent kinetic energy dissipation rate ( $\varepsilon$ ), which is a fundamental  
 parameter for turbulence closure models. The dissipation rate was estimated  
 from the HWA measurements as:

$$\varepsilon = \frac{15\nu}{U^2} \overline{\left(\frac{\partial u}{\partial t}\right)^2}, \quad (5)$$

364 by employing the isotropic approximation and Taylor's hypotheses of frozen tur-  
 365 bulence (Hinze, 1975). The vertical profile of  $\varepsilon$  agrees well with the production  
 366 rate of turbulent kinetic energy, here estimated as  $\mathcal{P} \approx -\overline{u'w'} \frac{\partial \bar{u}}{\partial z}$ . This shows  
 367 that in most of the boundary layer, the production and dissipation of turbulent  
 368 kinetic energy can be assumed to be in local equilibrium (Nironi et al., 2015).

369

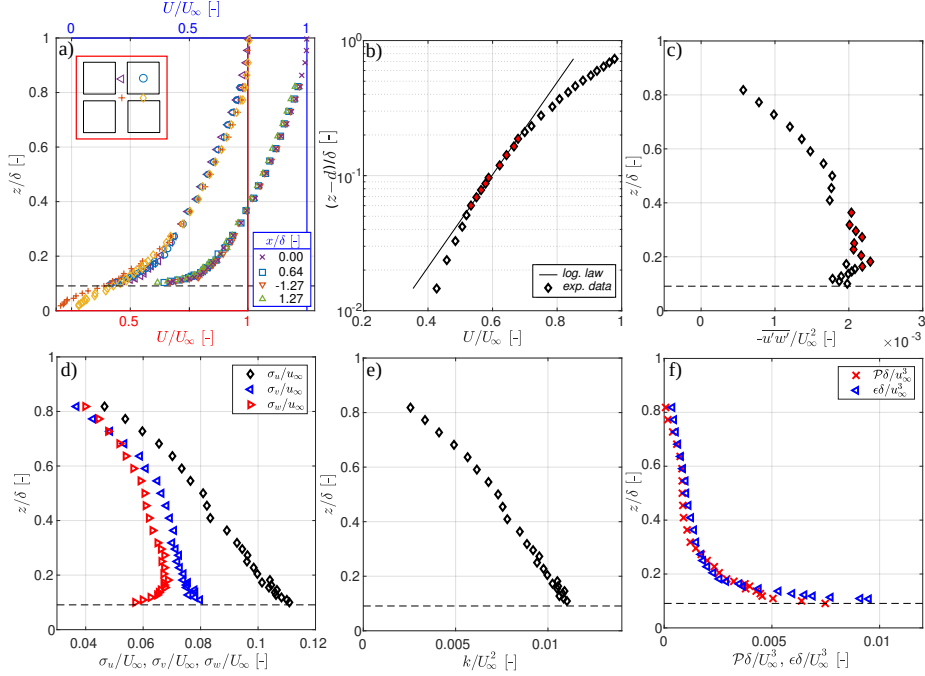


Figure 4: a) Mean velocity at 4 different position in a periodic unit (red bottom  $x$ -axis) and at 4 different distances along the streamwise direction of the wind tunnel (blue top  $x$ -axis). For the two groups of profiles, a vertical line corresponding the  $U/U_\infty = 1$  is reported. The horizontal dashed line corresponds to the canyon roof level ( $H$ ). b) Mean velocity obtained as average over four different positions. The line represents the logarithmic law with  $u_*/U_\infty = 0.051$ ,  $z_0/\delta = 9 \times 10^{-4}$ , and  $d/\delta = 0.085$ . The full symbols indicate the region where the logarithmic law applies. c) Reynolds stresses  $-\overline{u'w'}$ . The full symbols indicate the constant-stress region. d) Standard deviation of the three velocity components. e) Turbulent kinetic energy. f) Production and dissipation rate of turbulent kinetic energy.

### 370 3. Street canyon ventilation

#### 371 3.1. Mean concentration field

372 The mean concentration field inside the street canyon was characterized for  
373 the three configurations of tree density presented in Fig. 2. As mentioned above  
374 (Section 1.2), the concentration of ethane - released from the line source - was  
375 measured on around 1000 sampling points (for each configuration) distributed  
376 on a three-dimensional grid, by means of a Flame Ionization Detector. The non-  
377 dimensional concentration is expressed as  $\overline{C^*} = CU_\infty L_s \delta / Q_{et}$ , where  $C$  is the  
378 time-averaged concentration of ethane in each sampling point,  $L_s$  is the source  
379 length, and  $Q_{et}$  is the mass flow rate of ethane. In the following, the results are  
380 presented in two-dimensional sections obtained from linear interpolation of the  
381 measured data. For a complete visualisation of the concentration field inside  
382 the canyon refer to Section 2 of the Supplementary Material.

383 Figure 5 shows two cross-sections for each configuration of tree density. Pan-  
384 els a-c report the concentration field on a lateral cross-section ( $y/H \approx -15$ ),  
385 whereas panels d-f correspond to the central (around  $y/H \approx 0$ ) cross-section.  
386 Regardless of the presence of trees, a clear increase in the concentration from  
387 the downwind wall to the upwind wall can be observed in all the sections. This  
388 pattern is in accordance with previous studies (Gromke and Ruck, 2007, 2009)  
389 and evidences the action of the main recirculating cell of the velocity field inside  
390 the canyon: fresh air enters the canyon at the downwind wall and transports the  
391 pollutant (emitted in the centre of the street) to the upwind wall, where part  
392 accumulates at the lower corner, part is moved outside and part is entrained  
393 towards the downwind wall. The horizontal inhomogeneity of the concentration  
394 field results in a significant difference in air quality at the pedestrian level (i.e.  
395 at  $z/H = 0.2$ ). This difference is accentuated in the presence of trees: in a  
396 canyon without vegetation (Fig. 5.a and d), the concentration at the downwind  
397 wall is roughly 3 times lower than the one at the upwind wall, while in presence  
398 of trees this difference increases up to 8 times in the lateral section (Fig. 5.b  
399 and c). We also remark that, for the non-vegetated canyon, the concentration

field remains almost unchanged along the longitudinal axis of the canyon (panel a and d) while the presence of trees alters this behaviour: in both the *Half* and *Full* configurations, pollutant concentration in the central section (panel e and f) is significantly lower than in the lateral one (sections b and c).

To better visualize the spatial distribution of the concentration field, we show in Fig. 6 the horizontal section along the canyon axis, at  $z/H=0.5$ . The concentration gradient along the  $x$ -axis, from the downwind to the upwind wall, is clearly visible in all three configurations. As found above, this gradient is enhanced in the vegetated canyons. Analysing the concentration near the walls (see also the entire cross sections at  $x/H = 0.1$  and  $x/H = 1.9$  in the Supplementary Material), we find that this is due to an average increase in the concentration at the upwind wall in the vegetated canyons, rather than to a decrease of the concentration at the downwind wall, which remains almost constant in the different configurations. This result is in line with the study of Buccolieri et al. (2009) who found that the presence of trees lead to a significant increase in pollutant concentration at the upwind wall and slight to moderate decrease at the downwind wall.

Figure 6 also shows that along the longitudinal axis ( $y$ -axis), the concentration is almost homogeneous in the *Zero* configuration (panel a), except for the low values at the edges of the domain due to the limited length of the linear source. On the other hand, the homogeneity along the  $y$ -axis is lost when trees are added. In the *Full* configuration (panel c), it is possible to identify a region with lower concentration in the middle of the canyon and two nearly symmetric accumulation regions at its sides. In the *Half* configuration (panel b), the concentration field is even more heterogeneous and three accumulation regions can be identified. The same spatial distribution can be inferred from Fig. 7, where a vertical section in the middle of the canyon ( $x/H=1$ ) is represented. Again, we observe a homogeneous concentration field in the empty canyon, while pollution peaks are evident in the *Half* and *Full* configurations. Along the vertical axis, the concentration remains fairly constant. This is typical in the centre of the canyon and was already visible when focusing on vertical profiles at  $x/H=1$  in

431 Fig. 5. Moving towards the upwind wall (Fig. 8 shows the vertical section at  
 432  $x/H=0.15$ ), however, the concentration is greater at street level and a gradient  
 433 along the vertical axis emerges.

434 By averaging the concentration over the vertical direction ( $z$ ), we obtain (see  
 435 Fig. 9) the concentration profile along the longitudinal axis ( $y$ ), in the centre  
 436 of the canyon ( $x/H=1$ ). The profiles highlight the transition from an homo-  
 437 geneous concentration in the empty canyon to a spatial distribution exhibiting  
 438 pronounced peaks in the vegetated canyons. Furthermore, the increment in  
 439 the number of trees produces a decrease in the minimum concentration in the  
 440 centre of the canyon and a slight intensification of the maximum values. We  
 441 note that the cross-sections shown above in Fig. 5 were taken at the minimum  
 442 ( $y/H \approx 0$ ) and maximum (left side,  $y/H \approx -15$ ) concentration values for each  
 443 configuration.

444 Finally, from the characterization of the concentration field along the canyon  
 445 (Figs. 6-8), some observations on the local effect of trees on pollution can  
 446 be deduced. For both configurations with trees, the inhomogeneity along the  
 447 longitudinal axis ( $y$ ) is maintained along the  $x$ -axis (Fig. 6), both near the two  
 448 rows of trees ( $x/H \rightarrow 0$  and  $x/H \rightarrow 2$ ) and in the centre ( $x/H \rightarrow 1$ ). Furthermore,  
 449 the number of concentration peaks (2 and 3 in the *Full* and *Half* configurations,  
 450 respectively) and their spacing do not correspond to the number and spacing of  
 451 the trees, represented by dashed lines in Figs. 6 to 8. These two aspects, namely  
 452 the concentration inhomogeneity along the  $y$ -axis in the centre of the street and  
 453 the independence of the concentration peaks on tree pattern, suggest that the  
 454 variation of the concentration field along the canyon is not due to local effects  
 455 of trees acting as obstacles. Rather, the presence of trees seems to modify the  
 456 dynamics of flow and dispersion within the whole canyon leading to a different  
 457 spatial organization of the concentration field at the canyon-scale.

### 458 3.2. Vertical exchange velocity

459 While the previous section highlighted the effect of trees on the spatial pat-  
 460 tern of the concentration field, in this section we investigate the effect of veg-

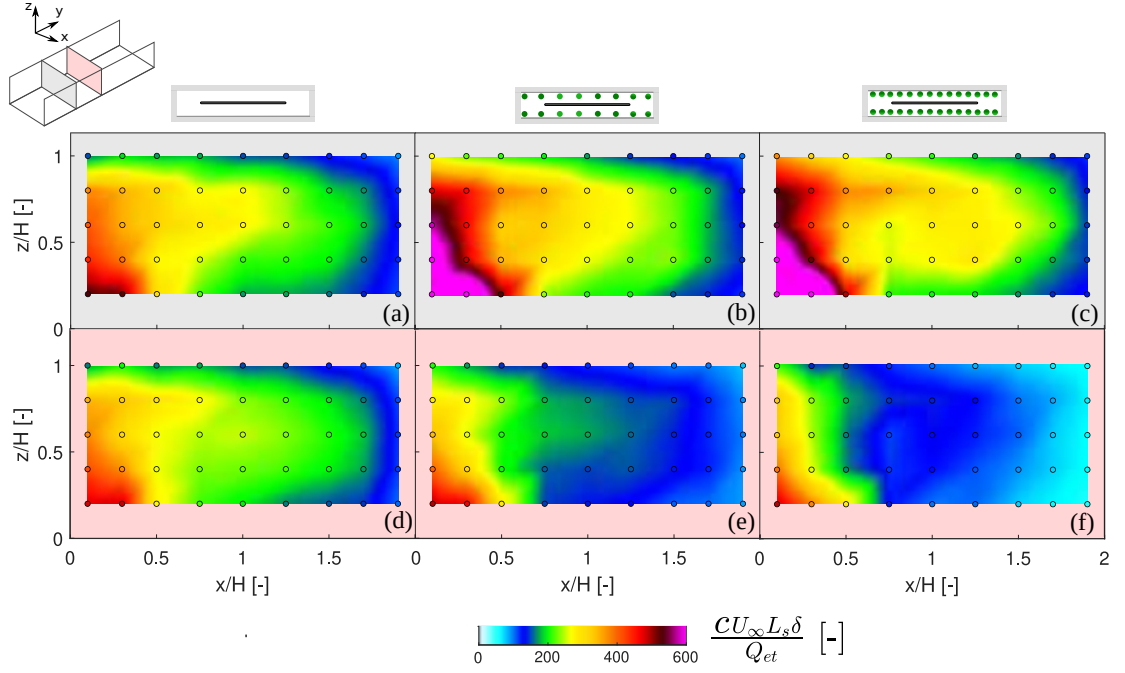


Figure 5: Mean concentration of the passive scalar on a lateral cross-section at  $y/H \approx -15$  (first line) and in the centre of the canyon  $y/H \approx -0$  (second line). *Zero* (a and d), *Half* (b and e) and *Full* (c and f) configurations are shown. Measurement points are reported as circles colored according to the measured value.

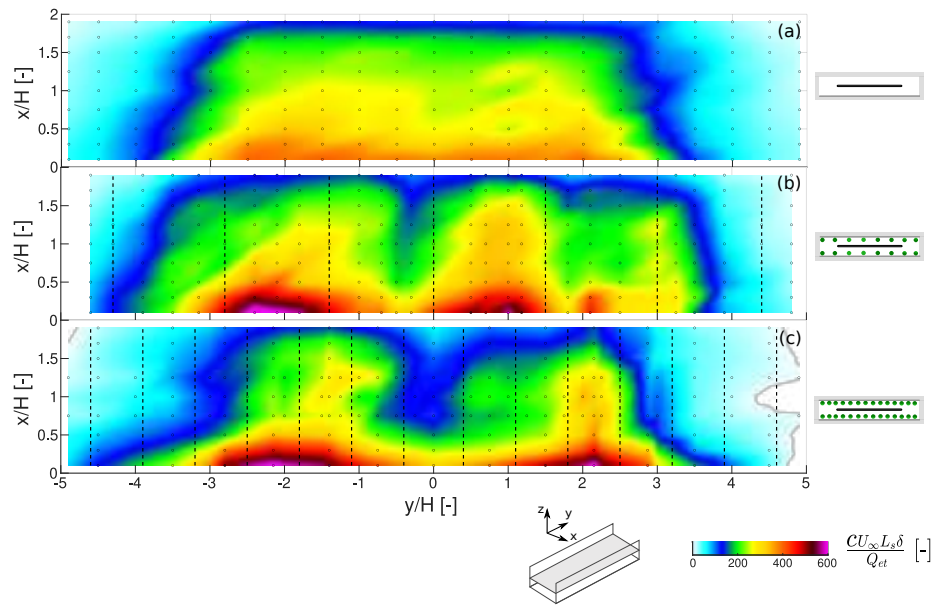


Figure 6: Mean concentration of the passive scalar on the horizontal section at  $z/H=0.5$ . *Zero* (a and d), *Half* (b and e) and *Full* (c and f) configurations are shown. The position of trees is represented by dashed lines. Measurement points are reported as circles colored according to the measured value.

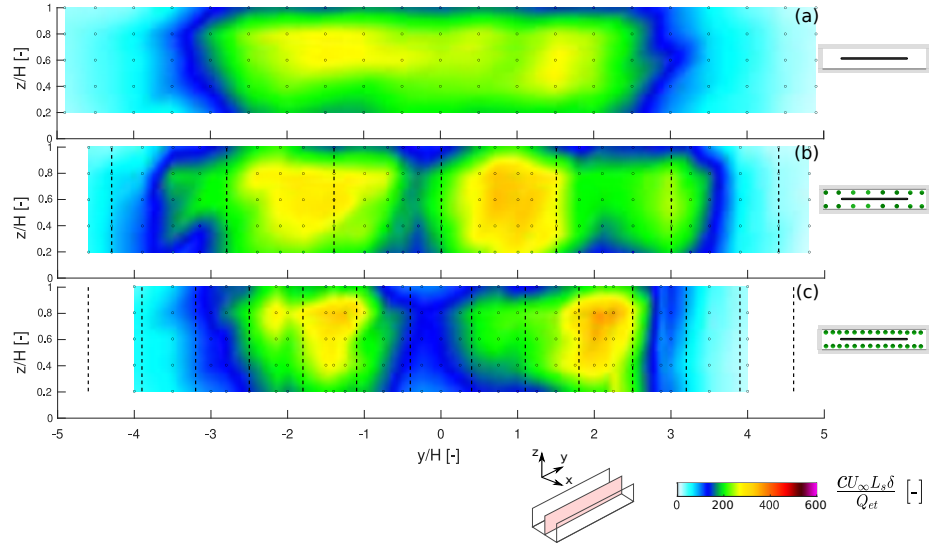


Figure 7: Mean concentration of the passive scalar on a vertical section at  $x/H=1$ . *Zero* (a and d), *Half* (b and e) and *Full* (c and f) configurations are shown. The position of trees is represented by dashed lines. Measurement points are reported as circles colored according to the measured value.

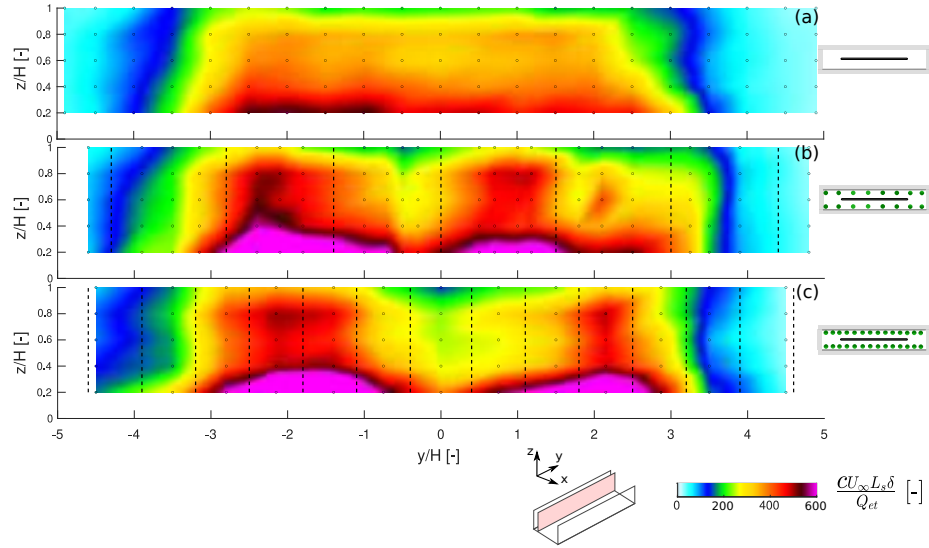


Figure 8: Mean concentration of the passive scalar on a vertical section at  $x/H=0.15$ . *Zero* (a and d), *Half* (b and e) and *Full* (c and f) configurations are shown. The position of trees is represented by dashed lines. Measurement points are reported as circles colored according to the measured value.



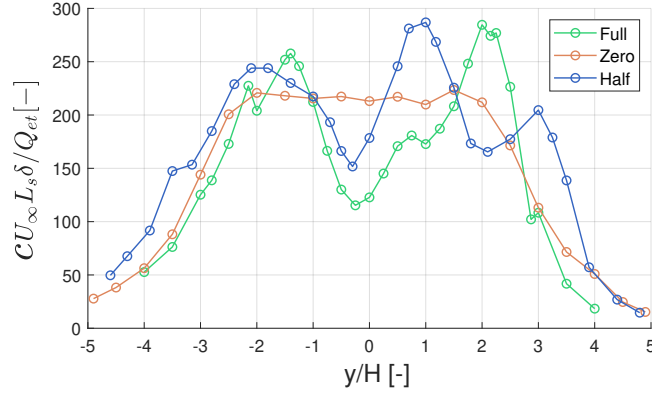


Figure 9: Concentration profile along the canyon axis ( $x/H = 1$ ) for the three configurations of tree density. Each point is obtained as the average concentration along the vertical axis ( $z$ ).

etation on the ventilation efficiency of the canyon. To this aim, we adopt a  
box model with one degree of freedom to evaluate the wash-out velocity of the  
canyon for the different configurations of tree density.

The canyon is described as a unique box with volume-averaged concentration and a domain boundary surface at the roof height (of area  $L \cdot W$ ). The mass balance for the canyon reads:

$$V \frac{\partial C_{vol}}{\partial t} + \int_{-L/2}^{L/2} \int_0^W [\overline{wc}]_{z=H} dx dy = Q_{et}, \quad (6)$$

where  $V$  is the volume of the canyon,  $Q_{et}$  is the mass flow rate of ethane at the source,  $C_{vol}$  is the mean concentration in the canyon, and  $\overline{wc}$  is the mass flux of passive scalar in the vertical direction. This latter is provided by the time-averaged product of the instantaneous vertical velocity  $w$  and concentration  $c$ . Following Soulhac et al. (2013), the vertical flux at roof level can be parametrized as the product of a bulk exchange velocity  $u_d$  and the difference between the concentration within the canyon ( $C_{vol}$ ) and the concentration in the external flow ( $C_{ext}$ ):

$$u_d(C_{vol} - C_{ext})WL = \int_{-L/2}^{L/2} \int_0^W [\overline{wc}]_{z=H} dy dx. \quad (7)$$

In steady state conditions (i.e.  $\partial C_{vol}/\partial t = 0$ ) and assuming that  $C_{ext}$  is neg-

ligible, Eqs. 6 and 7 can be combined, and the exchange velocity expressed as (Salizzoni et al., 2009):

$$u_d = \frac{Q_{et}}{C_{vol}WL}. \quad (8)$$

or in non-dimensional form as:

$$\frac{u_d}{U_\infty} = \frac{L_s\delta}{C_{vol}^*WL}, \quad (9)$$

where  $C_{vol}^*$  is the non-dimensional concentration averaged over the volume and  $L_s$  is the source length inside the volume. Thanks to this formulation, the vertical exchange velocity can be easily estimated from the quantities measured in the experiment: the flow rate at the source  $Q_{et}$  is imposed and monitored by a mass-flow rate controller, while the FID measurements inside the street canyon provide the average concentration in the entire volume ( $C_{vol}^*$ ).

In this regard, we recall that the choice of reproducing a canyon closed at the lateral edges was made to simplify the estimation of the exchange velocity  $u_d$ . Otherwise, in the case of a canyon with lateral street intersections, the mass balance in Eq. 6 would also include the flux of passive scalar along the longitudinal direction (i.e. the mass flux  $\overline{vc}$  provided by the transversal velocity  $v$  along  $y$  and integrated at the lateral boundaries of the domain, at  $y = -L/2$  and  $y = +L/2$ ). This additional term would also appear in Eqs. 8 and 9 and thus the estimation of  $u_d$  would require additional coupled measures of velocity and concentration. In the case of an infinitely long canyon (i.e. a canyon long as the wind-tunnel width), the balance would be applied to a reference volume since the fine characterization of the entire canyon length would be experimentally unfeasible. Also in this case, the estimate of the transverse mass flux at the lateral boundaries of the reference volume would be necessary to estimate  $u_d$ .

The mean concentration within the canyon was estimated with different spatial averaging techniques of the measurements: (i) the rough mean of the data, (ii) the mean weighted by the volume associated to each measurement point, and (iii) the mean over a regular concentration grid obtained from interpolation of the measurements. Table 1 reports the values of  $C^*$  obtained with these different methods. The greatest differences in the estimation of  $C^*$  are found

for the *Full* configuration, where the measurement grid is more irregular due to the presence of trees. In this case, the method adopted for the spatial integration can affect the results. Regardless the method used, we observe that the concentration average in the whole volume of the canyon remains substantially unchanged with the density of trees. This evidences that, while the spatial variation of the concentration field (Figs. 5-8) significantly varies due to the presence of trees, the average pollution level inside the canyon remains almost unaltered. This is a remarkable and unexpected result, as it is generally believed that trees, acting as aerodynamic obstacles, are responsible for the accumulation of pollutants in the street.

To better quantify the effect of trees on street canyon ventilation, we use Eq. 9 to estimate the exchange velocity  $u_d$ , starting from  $C_{vol}^*$ . The values of  $u_d$  are also presented in Table 1 and show, once again, that the influence of trees on ventilation efficiency is almost negligible. Furthermore, a trend of  $u_d$  with the vegetation density is absent, being the *Half* configuration the one exhibiting the lowest exchange rate. We also note that the estimated values of  $u_d$  are higher with respect to those found by Salizzoni et al. (2009), Soulhac et al. (2013), and Fellini et al. (2020) for a square cavity ( $H/W=1$ ), confirming that the enlargement of the cavity enhances canyon ventilation.

The values reported in Table 1 have been estimated considering the entire canyon as the reference volume. In Fig. 10, we show how the estimate of  $u_d$  varies as a function of the size of the reference volume. To this aim, we consider a reference volume centred at  $y=0$ , extended to the entire width ( $W$ ) and height ( $H$ ) of the canyon, but of variable length ( $L_{vol}$ ) along the longitudinal axis ( $y$ ). For the estimate of  $u_d$  by means of Eq. 9, the average concentration is estimated as the mean of the measurement data interpolated over a regular grid ('Interpolation' in Table 1) inside the reference volume, the source length  $L_s$  becomes the effective length included inside the reference volume ( $L'_s$  in Fig. 10) and the length  $L$  is replaced by  $L_{vol}$ . For the empty canyon, the exchange rate is almost unchanged as the reference volume increases. This is due to the homogeneity of the concentration field along  $y$ . In the *Full* configuration, the

		Rough	Weighted	Interpolation
$C_{vol}^* [-]$	<i>Zero</i>	155.45	162.50	155.43
	<i>Half</i>	198.61	178.75	178.74
	<i>Full</i>	178.76	143.00	162.50
$u_d/U_\infty [-]$	<i>Zero</i>	0.023	0.022	0.023
	<i>Half</i>	0.018	0.020	0.020
	<i>Full</i>	0.020	0.025	0.022

Table 1: Estimate of the volume-averaged (normalised) concentration  $C_{vol}^*$  for different spatial averaging techniques of the concentration inside the canyon: (i) rough mean, (ii) mean weighted on the reference volume of each measurement point, and (iii) mean of the three-dimensional interpolated concentration field. The corresponding values of the vertical exchange velocity  $u_d/U_\infty$ , calculated by means of Eq. 9, are also reported.

velocity  $u_d$  is greatly overestimated if a volume less than 40% of the total canyon is considered. The reason for this is that, according to the balance in Eq. 9, the lower concentration in the centre of the canyon results in a misleading high ventilation efficiency. The *Half* configuration shows an intermediate behaviour between the two. This analysis highlights the importance of a characterization of the concentration field on an extended volume for a correct evaluation of the overall ventilation efficiency. To analyse the effect of the presence of trees in the street, characterizing a single two-dimensional section or a limited volume in the middle of the canyon may lead to false conclusions.

#### 4. Discussion about the effect of lateral boundaries

As mentioned above, the canyon geometry with closed extremities was adopted to ensure a correct and straightforward estimate of the ventilation efficiency. However, this geometry is unusual compared to classic experimental investigations (and realistic urban geometries) and could raise the question that the lateral walls modify the flow field and therefore the dispersion process. For this reason, in this section we briefly discuss the effect of the lateral edges of the canyon on the concentration field. To do this, we compare the results pre-

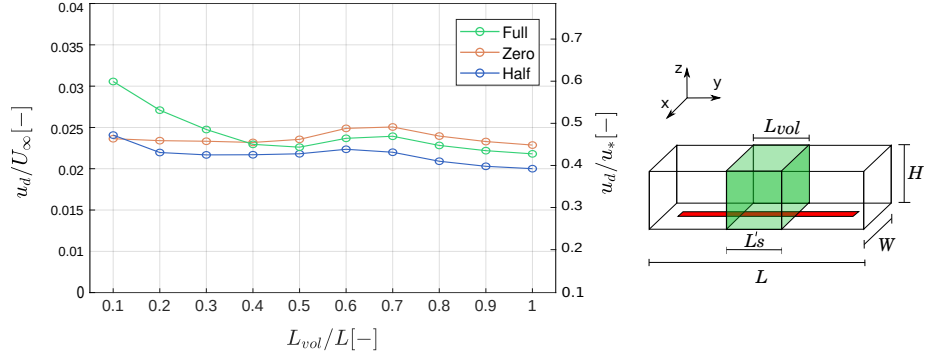


Figure 10: Estimate of the exchange velocity  $u_d$  as a function of the length ( $L_{vol}$ ) of the reference volume along the longitudinal axis of the canyon.

537 sented in the previous section with concentration measurements performed in  
 538 the same wind tunnel, with identical experimental conditions, but with slightly  
 539 different street geometries. We note that these measurements were performed  
 540 on a coarser grid with respect to that adopted for the investigation of the closed  
 541 canyon. While these measurements provide a qualitative description, a deep  
 542 analysis of the influence of lateral boundaries goes beyond the scope of this  
 543 paper.

544 In the first laterally-open geometry (Fellini, 2021), the reference canyon is  
 545 part of the network of streets that reproduces the idealized urban district. The  
 546 canyon is 50 cm long and is limited laterally by two street intersections (Fig.  
 547 11). Although the length-to-width ( $L/W$ ) ratio is lower and a regular array  
 548 of building is here present, the street geometry is similar to that adopted by  
 549 Gromke and Ruck (2007, 2009), where a laterally open canyon is reproduced.  
 550 Concentration measurements were performed over 4 cross-sections (sections 1 to  
 551 4) covering all the canyon length and placed at  $y/H \pm 1.88$  and  $y/H \pm 0.63$ . Re-  
 552 sults for an empty canyon and a canyon with a full density of trees are presented  
 553 in panels b and d of Fig. 11, respectively. The density of trees corresponds to  
 554 the *Full* configuration presented in Section 1.1. Panels c and e refer to the  
 555 canyon with closed lateral edges and report the concentration measured in the

cross-sections taken at the  $y/H$  positions closest to those of sections 1 to 4. Without trees, pollution levels are significantly lower in the open canyon (panel b) with respect to the laterally closed one (panel c). This is an expected result, as the formation of corner eddies near the intersections provide additional turbulent exchange that favours the canyon ventilation. Despite this variation in the pollution levels, we observe a similar trend for the concentration that remains almost unchanged along the longitudinal axis. The same observations can be made for the vegetated canyon: the presence of lateral intersections decreases the average concentration in the canyon but the trend along  $y$  is similar with open (panel d) and closed ends (panel e). In this case, sections 1 and 4 exhibit an increase in the concentration with respect to section 2 and 3. This trend is in line with the results found in Section 3.1 and suggests that trees induce a three-dimensional concentration field.

A similar comparison is performed for the geometry presented in Fig. 12.a. In this case, the canyon is extended to the entire width of the wind tunnel ( $W/H = 35$ ). The other geometrical properties of the canyon, as well as the experimental conditions, are the same as presented in Section 1.1. Concentration measurements are available in four cross-sections placed in the range at  $y/H \pm 1.07$  and  $y/H \pm 0.36$ . In both the *Zero* and *Full* configurations, the concentration values (panels b and d) are extremely similar to those found in the closed cavity (c and e). The concentration field remains constant along the axis of the canyon in the absence of trees (panel b), while in the *Full* configuration the concentration tends to increase in sections 1 and 4 which are located near the two peaks evident in Fig. 9. We note that the compared sections are not in exactly the same position along the  $y$ -axis, the differences being up to 3 cm. This may explain the slightly higher concentration in section 4 of the vegetated canyon (panels d and e). Furthermore, we highlight that in panels c and d the concentration distribution and the effect of the main canyon vortex can be visualized in greater detail due to the higher spatial resolution in the measurements.

The comparisons discussed in this section suggest that the results presented

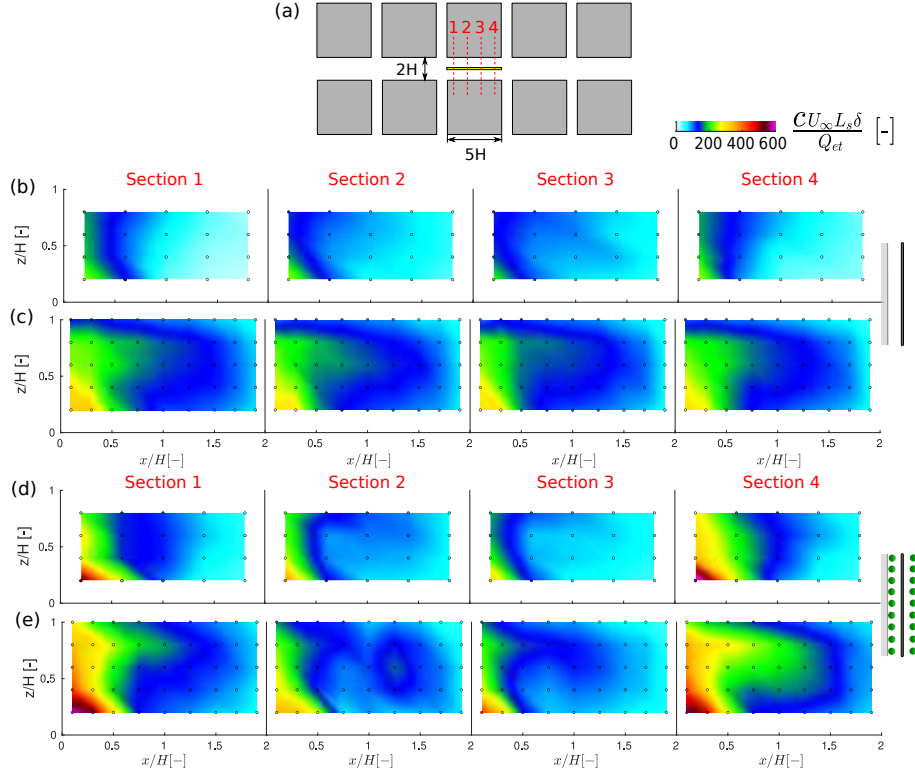


Figure 11: (a) Canyon with street intersections at the lateral extremities. Concentration in 4 cross-sections for the configuration without trees (b) and with dense trees (d). Comparison with the concentration in the closed cavity, in the *Zero* (e) and *Full* configurations.

in Sections 3.1 and 3.2 can be extended, with good approximation, to the standard case of an indefinitely long canyon. The closure of the lateral ends does not seem to alter the ventilation dynamics. The geometry with lateral intersections, on the other hand, presents more marked differences but the presence of trees seems, even in this case, to trigger the same transition from a two-dimensional to a three-dimensional concentration field.

## 5. Conclusions

We have investigated the effect of trees on ventilation efficiency and pollutant dispersion in an urban street canyon. In a wind tunnel, we have reproduced

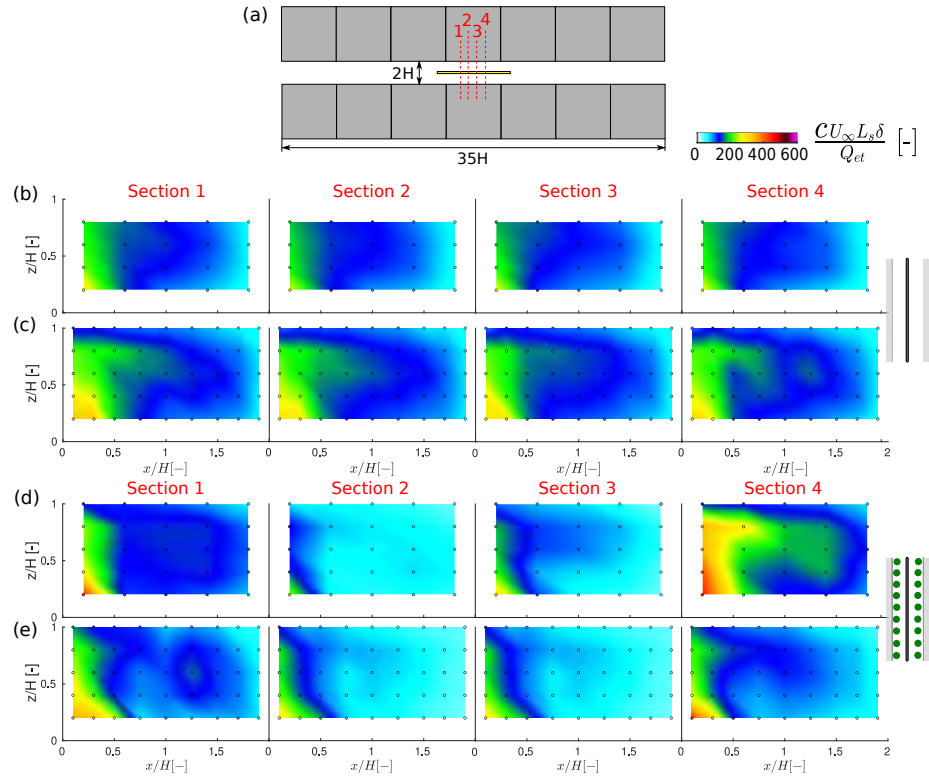


Figure 12: (a) Canyon extended to the width of the wind tunnel. Concentration in 4 cross-sections for the configuration without trees (b) and with dense trees (d). Comparison with the concentration in the closed cavity, in the *Zero* (e) and *Full* configurations.



596 a well-developed urban boundary layer over an idealized urban district simu-  
597 lated by an array of square blocks. We performed velocity measurements by  
598 means of an X-wire HWA in order to provide an accurate description of the  
599 flow field above the obstacles. The concentration field was measured by means  
600 of a FID within a reference street canyon modelled as a closed cavity oriented  
601 perpendicular with respect to the wind direction. Three different configurations  
602 of tree density were analysed: a non-vegetated canyon (*Zero* configuration), a  
603 canyon with two rows of sparse trees (*Half* configuration), and a canyon with  
604 two rows of dense trees (*Full* configuration). The model trees were aerodynam-  
605 ically characterized by means of their drag coefficient and crown porosity.

606 The results show that the concentration field is homogeneous along the lon-  
607 gitudinal axis of the canyon in the *Zero* configuration, and can be considered  
608 nearly two-dimensional. On the other hand, the vegetated streets present a  
609 remarkable three-dimensional spatial distribution of the concentration field. In  
610 particular, concentration peaks alternating with low polluted regions are ob-  
611 served along the canyon both in the *Half* and *Full* configurations and especially  
612 at pedestrian level. Moreover, the presence of trees lead to a significant increase  
613 of pollutant concentration at the upwind wall of the street, while the average  
614 concentration at the downwind wall is almost constant in the different configu-  
615 rations. Despite the great influence of trees on the spatial pattern of pollution,  
616 the average concentration in the entire volume of the canyon does not vary with  
617 the tree density, highlighting a compensation effect between the different regions  
618 of the street.

619 The ventilation efficiency of the canyon was assessed by estimating the bulk  
620 transfer velocity between the canyon and the boundary layer aloft. To this aim, a  
621 mass balance within the laterally closed canyon was performed. In line with the  
622 result about the mean concentration, the estimated velocity is almost constant  
623 among the three configurations, confirming that the vegetation density does not  
624 affect the overall ventilation efficiency. On the other hand, we demonstrated  
625 that the characterization of the concentration field over an extended reference  
626 volume is necessary to accurately estimate the transfer velocity when trees are

627 present.

628 Finally, we discussed the effect of the canyon lateral extremities on disper-  
629 sion dynamics. To this aim, we compared the outcomes from two experiments  
630 with slightly different canyon geometries. The presence of lateral street intersec-  
631 tions increases the ventilation of the canyon and therefore decreases the average  
632 pollution levels. However, both in the case of a non-vegetated canyon and in  
633 the presence of trees, the trend of the concentration along the longitudinal axis  
634 is similar to that found in this study. If we consider a canyon that extends to  
635 the entire width of the wind tunnel, the concentration pattern is quite similar  
636 to that observed in the configuration with closed ends and longitudinal mass  
637 fluxes are quite negligible. Therefore, the results of this study can be general-  
638 ized to the case of an infinitely long street canyon, which is a classical geometry  
639 adopted in both experimental and numerical studies.

640 To conclude, thanks to the detailed characterization of the concentration  
641 field, we showed that trees have a non-trivial effect on the spatial distribu-  
642 tion of the pollutant concentration, leading to a highly inhomogeneous scalar  
643 field and strong pollution gradients at the pedestrian level. This suggests that  
644 the presence of trees affect the turbulent flow field within the canyon. A new  
645 measurement campaign is currently underway to investigate the reasons for the  
646 formation of pollution peaks in the presence of trees. To this aim, we character-  
647 ize the structure of the turbulent flow field within the canyon and the vertical  
648 turbulent mass fluxes at the roof level. While the vertical exchange velocity  $u_d$   
649 is an average quantity over the entire volume, the analysis of the vertical tur-  
650 bulent fluxes should highlight whether there are spatial heterogeneities in the  
651 exchange between the canyon and the atmosphere.

652 Moreover, we found that the presence of two rows of trees does not inhibit  
653 the overall canyon ventilation. This result has important implications in prac-  
654 tice. The estimated value of the vertical exchange velocity can be included  
655 as a constant in parametric models that simulate pollutant dispersion in cities  
656 (McHugh et al., 1997; Soulhac et al., 2011; Fellini et al., 2019).

657 Finally, the huge dataset provided by this experimental study can be of great

use for the validation of numerical simulations. To this end, the characterization of the boundary layer and of the aerodynamic properties of trees (described in the Section 2) are fundamental information.

## Data availability

The experimental dataset is available on the website: [https://github.com/sfellini/Tree\\_alpha90\\_HW05.git](https://github.com/sfellini/Tree_alpha90_HW05.git). We provide the concentration data inside the canyon and the characterization of the flow field above the buildings.

## Acknowledgements

We would like to express our gratitude to Horacio Correia for the technical support in performing the wind tunnel experiments, and to Alessandro De Giovanni, Giacomo Balestrieri, and Lucas Mechinaud for taking part in the experimental campaign.

## References

- Abhijith, K., Kumar, P., Gallagher, J., McNabola, A., Baldauf, R., Pilla, F., Broderick, B., Di Sabatino, S., Pulvirenti, B., 2017. Air pollution abatement performances of green infrastructure in open road and built-up street canyon environments—a review. *Atmospheric Environment* 162, 71–86.
- Allegrini, J., Dorer, V., Carmeliet, J., 2013. Wind tunnel measurements of buoyant flows in street canyons. *Building and Environment* 59, 315–326.
- Bozovic, R., Maksimovic, C., Mijic, A., Smith, K., Suter, I., Van Reeuwijk, M., 2017. Blue green solutions. a systems approach to sustainable and cost-effective urban development .
- Buccolieri, R., Carlo, O.S., Rivas, E., Santiago, J.L., Salizzoni, P., Siddiqui, M.S., 2022. Obstacles influence on existing urban canyon ventilation and air pollutant concentration: A review of potential measures. *Building and Environment* , 108905.

684 Buccolieri, R., Gromke, C., Di Sabatino, S., Ruck, B., 2009. Aerodynamic  
685 effects of trees on pollutant concentration in street canyons. *Science of the*  
686 *Total Environment* 407, 5247–5256.

687 Buccolieri, R., Salim, S.M., Leo, L.S., Di Sabatino, S., Chan, A., Ielpo, P.,  
688 de Gennaro, G., Gromke, C., 2011. Analysis of local scale tree-atmosphere  
689 interaction on pollutant concentration in idealized street canyons and appli-  
690 cation to a real urban junction. *Atmospheric Environment* 45, 1702–1713.

691 Busca, F., Revelli, R., 2022. Green areas and climate change adaptation in a  
692 urban environment: The case study of “le vallere” park (turin, italy). *Sus-*  
693 *tainability* 14, 8091.

694 Carpentieri, M., Hayden, P., Robins, A.G., 2012. Wind tunnel measurements of  
695 pollutant turbulent fluxes in urban intersections. *Atmospheric Environment*  
696 46, 669–674.

697 Castro, I., Robins, A., 1977. The flow around a surface-mounted cube in uniform  
698 and turbulent streams. *Journal of fluid Mechanics* 79, 307–335.

699 Chen, J., Black, T., Novak, M., Adams, R., 1995. A wind tunnel study of  
700 turbulent airflow in forest clearcuts. *Wind and trees* , 71–87.

701 Cheng, H., Hayden, P., Robins, A., Castro, I., 2007. Flow over cube arrays  
702 of different packing densities. *Journal of Wind Engineering and Industrial*  
703 *Aerodynamics* 95, 715–740.

704 Comte-Bellot, G., 1976. Hot-wire anemometry. *Annual review of fluid mechanics*  
705 8, 209–231.

706 Fackrell, J., 1980. A flame ionisation detector for measuring fluctuating concen-  
707 tration. *Journal of Physics E: Scientific Instruments* 13, 888.

708 Fellini, S., 2021. Modelling pollutant dispersion at the city and street scales.  
709 Ph.D. thesis. Politecnico di Torino & École Centrale de Lyon.

710 Fellini, S., Ridolfi, L., Salizzoni, P., 2020. Street canyon ventilation: Combined  
711 effect of cross-section geometry and wall heating. *Quarterly Journal of the*  
712 *Royal Meteorological Society* .

713 Fellini, S., Salizzoni, P., Soulhac, L., Ridolfi, L., 2019. Propagation of toxic  
714 substances in the urban atmosphere: A complex network perspective. *Atmo-*  
715 *spheric Environment* 198, 291–301.

716 Garbero, V., Salizzoni, P., Soulhac, L., 2010. Experimental study of pollutant  
717 dispersion within a network of streets. *Boundary-layer meteorology* 136, 457–  
718 487.

719 Georgakis, C., Santamouris, M., 2017. Determination of the surface and canopy  
720 urban heat island in athens central zone using advanced monitoring. *Climate*  
721 5, 97.

722 Gromke, C., Blocken, B., 2015. Influence of avenue-trees on air quality at the  
723 urban neighborhood scale. part i: Quality assurance studies and turbulent  
724 schmidt number analysis for rans cfd simulations. *Environmental Pollution*  
725 196, 214–223.

726 Gromke, C., Buccolieri, R., Di Sabatino, S., Ruck, B., 2008. Dispersion study  
727 in a street canyon with tree planting by means of wind tunnel and numerical  
728 investigations–evaluation of cfd data with experimental data. *Atmospheric*  
729 *Environment* 42, 8640–8650.

730 Gromke, C., Jamarkattel, N., Ruck, B., 2016. Influence of roadside hedgerows  
731 on air quality in urban street canyons. *Atmospheric environment* 139, 75–86.

732 Gromke, C., Ruck, B., 2007. Influence of trees on the dispersion of pollutants  
733 in an urban street canyon - Experimental investigation of the flow and con-  
734 centration field. *Atmospheric Environment* 41, 3287–3302.

735 Gromke, C., Ruck, B., 2008. Aerodynamic modelling of trees for small-scale  
736 wind tunnel studies. *Forestry* 81, 243–258.

737 Gromke, C., Ruck, B., 2009. On the impact of trees on dispersion processes of  
738 traffic emissions in street canyons. *Boundary-Layer Meteorology* 131, 19–34.

739 Gromke, C., Ruck, B., 2012. Pollutant concentrations in street canyons of differ-  
740 ent aspect ratio with avenues of trees for various wind directions. *Boundary-*  
741 *Layer Meteorology* 144, 41–64.

742 Guan, D., Zhang, Y., Zhu, T., 2003. A wind-tunnel study of windbreak drag.  
743 *Agricultural and forest meteorology* 118, 75–84.

744 Hinze, J., 1975. *Turbulence*, Second edition. McGraw-Hill, New York.

745 Huang, Y.d., Li, M.z., Ren, S.q., Wang, M.j., Cui, P.y., 2019. Impacts of tree-  
746 planting pattern and trunk height on the airflow and pollutant dispersion  
747 inside a street canyon. *Building and Environment* 165, 106385.

748 Irwin, H., 1981. The design of spires for wind simulation. *Journal of Wind*  
749 *Engineering and Industrial Aerodynamics* 7, 361 – 366. doi:[https://doi.](https://doi.org/10.1016/0167-6105(81)90058-1)  
750 [org/10.1016/0167-6105\(81\)90058-1](https://doi.org/10.1016/0167-6105(81)90058-1).

751 Janhäll, S., 2015. Review on urban vegetation and particle air pollution–  
752 deposition and dispersion. *Atmospheric environment* 105, 130–137.

753 Li, H., Zhao, Y., Sützl, B., Kubilay, A., Carmeliet, J., 2022. Impact of green  
754 walls on ventilation and heat removal from street canyons: Coupling of ther-  
755 mal and aerodynamic resistance. *Building and Environment* 214, 108945.

756 Litschke, T., Kuttler, W., 2008. On the reduction of urban particle concentration  
757 by vegetation—a review. *Meteorologische Zeitschrift* 17, 229–240.

758 Livesley, S., McPherson, E.G., Calfapietra, C., 2016. The urban forest and  
759 ecosystem services: impacts on urban water, heat, and pollution cycles at the  
760 tree, street, and city scale. *Journal of environmental quality* 45, 119–124.

761 Manickathan, L., Defraeye, T., Allegrini, J., Derome, D., Carmeliet, J., 2018.  
762 Comparative study of flow field and drag coefficient of model and small natural  
763 trees in a wind tunnel. *Urban Forestry & Urban Greening* 35, 230–239.

764 Marro, M., Gamel, H., Méjean, P., Correia, H., Soulhac, L., Salizzoni, P.,  
765 2020. High-frequency simultaneous measurements of velocity and concen-  
766 tration within turbulent flows in wind-tunnel experiments. *Experiments in*  
767 *Fluids* 61, 1–13.

768 Marucci, D., Carpentieri, M., 2019. Effect of local and upwind stratification on  
769 flow and dispersion inside and above a bi-dimensional street canyon. *Building*  
770 *and Environment* 156, 74–88.

771 McHugh, C., Carruthers, D., Edmunds, H., 1997. Adms–urban: an air quality  
772 management system for traffic, domestic and industrial pollution. *Interna-*  
773 *tional Journal of Environment and Pollution* 8, 666–674.

774 Merlier, L., Jacob, J., Sagaut, P., 2018. Lattice-boltzmann large-eddy simula-  
775 tion of pollutant dispersion in street canyons including tree planting effects.  
776 *Atmospheric Environment* 195, 89–103.

777 Meroney, R.N., 1968. Characteristics of wind and turbulence in and above model  
778 forests. *Journal of Applied Meteorology* 7, 780–788.

779 Meroney, R.N., 1980. Wind-tunnel simulation of the flow over hills and complex  
780 terrain. *Journal of Wind Engineering and Industrial Aerodynamics* 5, 297–  
781 321.

782 Meroney, R.N., Pavageau, M., Rafailidis, S., Schatzmann, M., 1996. Study of  
783 line source characteristics for 2-d physical modelling of pollutant dispersion  
784 in street canyons. *Journal of wind Engineering and industrial Aerodynamics*  
785 62, 37–56.

786 Moonen, P., Gromke, C., Dorer, V., 2013. Performance assessment of large eddy  
787 simulation (les) for modeling dispersion in an urban street canyon with tree  
788 planting. *Atmospheric environment* 75, 66–76.

789 Murena, F., Mele, B., 2016. Effect of balconies on air quality in deep street  
790 canyons. *Atmospheric Pollution Research* 7, 1004–1012.

791 Nironi, C., Salizzoni, P., Marro, M., Mejean, P., Grosjean, N., Soulhac, L.,  
792 2015. Dispersion of a passive scalar fluctuating plume in a turbulent bound-  
793 ary layer. part i: Velocity and concentration measurements. *Boundary-layer*  
794 *meteorology* 156, 415–446.

795 Oliveira, S., Andrade, H., Vaz, T., 2011. The cooling effect of green spaces as a  
796 contribution to the mitigation of urban heat: A case study in lisbon. *Building*  
797 *and environment* 46, 2186–2194.

798 Pavageau, M., Schatzmann, M., 1999. Wind tunnel measurements of concen-  
799 tration fluctuations in an urban street canyon. *Atmospheric Environment* 33,  
800 3961–3971.

801 Rafailidis, S., 1997. Influence of building areal density and roof shape on the  
802 wind characteristics above a town. *Boundary-layer meteorology* 85, 255–271.

803 Raupach, M., Hughes, D., Cleugh, H., 2006. Momentum absorption in rough-  
804 wall boundary layers with sparse roughness elements in random and clustered  
805 distributions. *Boundary-Layer Meteorology* 120, 201–218.

806 Salim, S.M., Cheah, S.C., Chan, A., 2011. Numerical simulation of dispersion  
807 in urban street canyons with avenue-like tree plantings: comparison between  
808 rans and les. *Building and Environment* 46, 1735–1746.

809 Salizzoni, P., Soulhac, L., Mejean, P., 2009. Street canyon ventilation and  
810 atmospheric turbulence. *Atmospheric Environment* 43, 5056–5067.

811 Salizzoni, P., Soulhac, L., Mejean, P., Perkins, R.J., 2008. Influence of a two-  
812 scale surface roughness on a neutral turbulent boundary layer. *Boundary-layer*  
813 *meteorology* 127, 97–110.

814 Soulhac, L., Perkins, R.J., Salizzoni, P., 2008. Flow in a street canyon for any  
815 external wind direction. *Boundary-Layer Meteorology* 126, 365–388.

816 Soulhac, L., Salizzoni, P., Cierco, F.X., Perkins, R., 2011. The model SIRANE  
817 for atmospheric urban pollutant dispersion; part I, presentation of the model.  
818 *Atmospheric Environment* 45, 7379–7395.



- 819 Soulhac, L., Salizzoni, P., Mejean, P., Perkins, R., 2013. Parametric laws to  
820 model urban pollutant dispersion with a street network approach. *Atmo-*  
821 *spheric Environment* 67, 229–241.
- 822 Stacey, G., Belcher, R., Wood, C., Gardiner, B., 1994. Wind flows and forces  
823 in a model spruce forest. *Boundary-Layer Meteorology* 69, 311–334.
- 824 Tritton, D.J., 2012. *Physical fluid dynamics*. Springer Science & Business Media.
- 825 Tutu, N.K., Chevray, R., 1975. Cross-wire anemometry in high intensity turbu-  
826 lence. *Journal of Fluid Mechanics* 71, 785–800.
- 827 Velarde, J.G., Blanco, J.H., Aliseda, J.M., 2018. Estimation of optical porosity  
828 or canopy structure of two species of tree with hemispherical and vertical  
829 images. *WSEAS Transactions on Environment and Development* 14, 112–  
830 124.
- 831 Vidali, C., Marro, M., Correia, H., Gostiaux, L., Jallais, S., Houssin, D.,  
832 Vyazmina, E., Salizzoni, P., 2022. Wind-tunnel experiments on atmospheric  
833 heavy gas dispersion: Metrological aspects. *Experimental Thermal and Fluid*  
834 *Science* 130, 110495.
- 835 Vos, P.E., Maiheu, B., Vankerkom, J., Janssen, S., 2013. Improving local air  
836 quality in cities: to tree or not to tree? *Environmental pollution* 183, 113–122.
- 837 Vranckx, S., Vos, P., Maiheu, B., Janssen, S., 2015. Impact of trees on pollutant  
838 dispersion in street canyons: A numerical study of the annual average effects  
839 in antwerp, belgium. *Science of the Total Environment* 532, 474–483.